Veterinary Research

RESEARCH ARTICLE

Open Access

Astrocyte-derived MMP-9 is a key mediator of pseudorabies virus penetration of the blood–brain barrier and tight junction disruption

Ying Zhang[1*], Xianghua Shu[1*], Ying Zhang[1], Chunlian Song[1†], Yi Wu[1], Kesi Cui[1], Xue Zhang[1], Yalong Sun[1], Hong Shen[1], Qianfei Wei[1], Jianqin Li[1] and Yue Shu[2]

Abstract

Pseudorabies virus (PRV) infection leads to viral encephalitis and neurological damage in mice, causing significant neurological symptoms and brain damage. This study aimed to investigate the cellular mechanisms of PRV-induced encephalopathy and the role of matrix metalloproteinase-9 (MMP-9) in blood–brain barrier (BBB) disruption. We found that PRV infection increased the number of astrocytes and induced a phenotypic shift from the A2 to the A1 subtype, which was associated with increased secretion of MMP-9. MMP-9 was identified as a critical mediator of PRV-induced BBB disruption, as it degrades collagen VI, leading to BBB damage. PRV was shown to penetrate the BBB via a paracellular pathway, and MMP-9 deletion reversed this damage, mitigating tight junction injury. Additionally, PRV infection caused an "inflammatory storm" in the central nervous system (CNS), with increased levels of the chemokines CCL-3, CCL-4, and CCL-5; the cytokines IL-6 and IL-18; and TNF-α. The expression of INF-γ was significantly decreased. In conclusion, PRV infection disrupts the BBB and induces an inflammatory response in the CNS, with MMP-9 playing a key role in mediating BBB damage. These findings provide insights into the pathogenesis of PRV-induced encephalopathy and potential therapeutic targets for viral encephalitis.

Keywords Pseudorabies virus, matrix metalloproteinase-9, blood–brain barrier, tight junctions, astrocytes

Introduction

In recent years, there have been a growing number of studies on human encephalitis or endophthalmitis caused by pseudorabies virus (PRV) [1, 2]. Upon human PRV infection, the initial symptoms include upper respiratory tract infection, followed by fever and potentially meningoencephalitis [1, 3–5]. PRV has emerged as a new zoonotic pathogen that requires increased investigation, and its potential impact should not be underestimated. PRV primarily infects the nervous system and frequently invades the trigeminal ganglion. When the body is stimulated by PRV, the latent virus can be reactivated through latency-reactivation [6]. The ability of PRV to evade host immune attacks through latency and spread during activation is predominantly why the current prevention and control techniques cannot completely eradicate the virus.

To successfully invade the central nervous system (CNS), neurotropic viruses employ various strategies, one of which involves destruction of the blood–brain barrier (BBB). The BBB is a crucial physiological defence mechanism that protects the CNS from infiltration by

Handling editor: Stéphane Biacchesi.

†Ying Zhang and Chunlian Song contributed equally to this study. The order of authorship is determined by primary responsibility.

*Correspondence:
Ying Zhang
Xianghua Shu
ynndsxh@ynau.edu.cn
[1] Present Address: College of Veterinary Medicine of Yunnan Agricultural University, Kunming 650201, Yunnan Province, China
[2] The Faculty of Science and Mathematics, Auburn University, Auburn, AL, USA

foreign substances. Astrocytes are an important part of the neurovascular unit, providing support and signals to the BBB under both physiological and pathological conditions [7]. However, some neurotropic viruses can invade the CNS by disrupting the BBB and dysregulating various molecular pathways in the host. Various factors regulate the entry of neurotropic viruses into the CNS, including adhesion molecules (platelet endothelial cell adhesion molecules [PECAM], CD99, vascular endothelial [VE]-cadherin, and junctional adhesion molecules [JAM]-A, B, and C), chemokines (CXC, CC, and CX3C), and matrix metalloproteinases (MMPs; MMP-2 and MMP-9) [8].

MMP-9 plays a crucial role in the pathogenesis of several nervous system diseases. Furthermore, MMP-9 plays a key role in BBB disruption, oedema formation, and disintegration of neurovascular units [9]. Recently, there has been a significant increase in research on the roles of MMP-9, and it is no longer believed to be limited to cerebrovascular diseases such as stroke [10], subarachnoid haemorrhage [11], and atherosclerosis [12]. Researchers have shifted their focus to the role of MMP-9 in CNS infections caused by microorganisms, particularly viruses. However, the role of MMP-9 in PRV invasion of the CNS and the mechanisms underlying BBB damage remain unknown.

In this study, we explored the role of MMP-9 in the penetration of the BBB by PRV and determined the pathways involved in PRV invasion to identify potential targets and strategies for the prevention and control of PRV.

Materials and methods

Animals, cells, and viruses

Ninety-six 8-week-old Kunming SPF mice weighing 32–46 g were purchased from Kunming Medical University for this study (laboratory animal production licence number: SCXK (Yunnan) K2020 0004)).

bEnd.3 (CL-0598, Procell) and C8-D1A (CL-0506, Procell) cells were grown at 37 ℃ with 5% CO_2 in Dulbecco's modified Eagle's medium (DMEM; 12110, Solarbio) supplemented with 10% foetal bovine serum (FBS; A5669701, Gibco), 100 U/mL penicillin, and 100 U/mL streptomycin sulphate (15140122, Thermo Fisher).

The PRV solution was provided by the Key Laboratory for the Prevention and Control of Important Livestock and Poultry Diseases of Universities in Yunnan Province [13].

Animal ethics statement

All experiments performed in this study were approved by the International Animal Care and Use Committee of Yunnan Agricultural University (permission code: 202405003; date of approval: January 1, 2022). This study complied with the guidelines of the Institutional Administration and Ethics Committee for Laboratory Animals.

Grouping and sampling

Ninety-six Kunming SPF mice were randomly allocated to the control or experimental groups. The control group ($n=24$) received 35 μL of normal saline. The experimental group ($n=72$) was administered 35 μL of PRV through a nasal drip (6.6×10^6 PFU/mL). The experimental group was further divided into three subgroups based on the duration of infection (24, 48, and 72 h), each containing 24 mice. After the test period, the mice were anaesthetized by intraperitoneal injection of 45 mg/kg pentobarbital sodium for subsequent experiments.

Haematoxylin and eosin staining

Brain tissues were collected from PRV-infected mice and stored in 10% paraformaldehyde. The tissue samples were cut into 5 mm×5 mm×3 mm sections and processed according to standard procedures [14]. Formalin-fixed, paraffin-embedded tissue sections with a thickness of 5 μm were stained with haematoxylin and eosin (H&E) for microscopic examination.

Modified neurological severity score (mNSS)

The mNSS scoring method [15] was used to score the degree of neurological function damage in the mice, and the scoring method is shown in Table 1.

Transmission electron microscopy

Ultrastructural analysis was performed as described previously [16]. Briefly, hippocampal coronary sections obtained from the mice were carefully dissected and fixed in 2.5% glutaraldehyde at 4 °C for 2 h. The samples were treated with 1% osmium tetroxide in 0.1 M cacodylate buffer for 1 h, and 1% uranyl acetate was added, followed by dehydration in ethanol. The samples were embedded in epoxy resin, sectioned (90 nm), and placed on carbon-coated copper grids. After being stained with uranyl acetate and lead citrate, the samples were visualized using

Table 1 Modified neurological severity scores

Score	Left forepaw disability	Body swing	Rightward rotation	Depressed level of consciousness	Unresponsive to stimulation or death
0	–	–	–	–	–
1	+	–	–	–	–
2	+	+	–	–	–
3	+	+	+	–	–
4	+	–	–	+	–
5	+	–	–	–	+

a transmission electron microscope (HT7800, Hitachi, Japan).

Dry–wet method

After deep anaesthetization with pentobarbital sodium (45 mg/kg), the mice were decapitated, and intact brain tissue was removed and placed on clean filter paper to remove surface exudates and blood. After the wet weight (WW) was obtained, the tissues were placed in an oven at 95 ℃ and the dry weight (DW) was measured after continuous heating for 24 h. The brain wet/dry (W/D) weight ratios were calculated using the following formula:

$$W/D = \frac{WW - DW}{WW} \times 100\%$$

Analysis of BBB permeability in vivo using Evans blue staining

Changes in BBB permeability in vivo were assessed using Evans blue dye (EBD), a marker of albumin extravasation, as previously described [17]. Briefly, the mice were anaesthetized with intraperitoneal injection of pentobarbital sodium (45 mg/kg) and intravenously injected with 2% EBD solution in saline (4 mL/kg). The EBD was left to circulate for 45 min, and the mice were then perfused transcranially with saline until the fluid in the right atrium turned colourless. The brain and other major organs were removed and weighed, and the dye was extracted with formamide at 56 °C for 48 h. The dye concentration was quantified spectrophotometrically at 620 nm and normalized to the weight of the tissue.

Molecular docking

The human proteins encoding the MMP-9 and collagen VI genes were obtained from the PDB database. The mol 2 format of the corresponding proteins was obtained through the TCMSP database, and the proteins and compounds were imported into Discovery Studio 2016 Client software for molecular docking.

Co-immunoprecipitation (Co-IP)

Eight micrograms of antibody and protein lysate containing 1 mg of protein were added to each system and incubated overnight at 4 ℃ with rotation. A total of 160 μL of suspended magnetic beads was added to a 1.5 mL microcentrifuge tube. The beads were washed three times with 0.1% PBST solution, the preprepared antigenicity antibody complexes were added to the beads, and the immune complexes were captured by incubation overnight at 4 ℃ on a suspension instrument (Table 2). After incubation, the protein supernatant was discarded, and the mixture was cleared with PBST and salt solution. The beads were washed three times, and 1 × SDS–PAGE loading buffer was added for high-temperature denaturation elution. The eluted proteins were used for subsequent Western blot (WB) experiments.

qRT-PCR analysis

Total DNA was extracted using a TaKaRa MiniBEST Viral RNA/DNA Extraction Kit (9766; TaKaRa, China). Total RNA was extracted using TRIzol Reagent (9767, TaKaRa) and reverse transcribed using a PrimeScript RT reagent kit (RR047A, TaKaRa). qRT-PCR was performed using a QuantStudio 6 Flex Real-Time PCR System with SYBR Premix Ex Taq (RR820A; TaKaRa). The data were normalized to the expression of the control gene β-actin. The transcripts were quantified using the $2^{-\Delta\Delta Ct}$ method. The primers used for qRT-PCR analysis are shown in Table 3.

Table 2 Antibodies used in the present study

Antibody	Source	Host	Purpose	Dilution
MMP-9	27306–1-AP, Proteintech	Rabbit	Co-ip	1:600
Collagen VI	AF0510, Affinity	Rabbit	Co-ip	1:500
MMP-9	ab76003, Abcam	Rabbit	IF	1:250
Collagen V	352500, Affinity	Rabbit	WB	1:500
ZO-1	AF5145, Affinity	Rabbit	WB	1:1000
Occludin	AF4605, Affinity	Rabbit	WB	1:1000
β-actin	8457, Cell Signalling	Rabbit	WB	1:1000
GFAP	ab7260, Abcam	Rabbit	IF	1:500
CD31	28083–1-AP, Proteintech	Rabbit	IF	1:200
Goat Anti-Rabbit IgG H&L (Alexa Fluor® 488)	ab150077, Abcam	Goat	IF	1:100
Goat Anti-Rabbit IgG H&L (Alexa Fluor® 647) preadsorbed	ab150083, Abcam	Goat	IF	1:100
Goat Anti-Rabbit IgG H&L (HRP)	ab205718, Abcam	Goat	WB	1:8000

Table 3 Sequences of the oligonucleotides used in RT–PCR

Name	Forward (5′–3′)	Reverse (5′–3′)	Probe (5′–3′)
Mouse			
Callagen V	GCAAGGTGTATGAATCTGTGCT	GTCAAGGTAACAAAGAGTGCCA	
ZO-1	GATGTTTATGCGGACGGTGG	AAATCCAAACCCAGGAGCCC	
Occludin	GGCAAGCGATCATACCCAGA	TTCCTGCTTTCCCCTTCGTG	
MMP-9	CTGGACAGCCAGACACTAAAG	CTCGCGGCAAGTCTTCAGAG	
β-actin	GTGACGTTGACATCCGTAAAGA	GCCGGACTCATCGTACTCC	
gE	CCGAGGACGAGTTCAGCA	GGCCCATTCGTCACTTCCG	ACCAGACGTCGAAGCCGGA
Cell			
Callagen V	GGGCGAGCATTCGGTCTTTA	AGAATCAAGCCCACCCAACC	
ZO-1	TAAACCTCCAAGTGCTTCCCT	CTTCAGGTGGCTTGACTTGAG	
Occludin	ATGGGAGTCAACCCAACTGC	ATGGGAGTCAACCCAACTGC	
MMP-9	GATCAGCCGGGAACGTATCTG	GTATGAGTCCCTCTCGCTCCC	
β-actin	GTGACGTTGACATCCGTAAAGA	GCCGGACTCATCGTACTCC	
CCL-3	TGGAATTTGCCGTCCATAGGAG	GTTGTAGTAGCTGTCCTGTCCT	
CCL-4	CACCTCCCGGAAGATTCATCG	GGCCAGTTTCCTGTCATTCC	
CCL-5	AGTGGTGTCCGAGCCATCTG	CCGAGGTAGACAACAGCAGAC	
IL-6	TTCAAACAAGAGGTGAGTGCG	AAGTGCTGCTACCCTGAGATG	
IL-18	GCTGAAATCCGAATTCCTACAC	TACTTCTCGTTCCTACCTTTCAG	
TNF-α	GGAGGGAGAACAGCAACTCC	GCCAGTGTATGAGAGGGACG	
INF-γ	GTAAACGCTCTGAGGAGGAGG	CTAACACACAACCTCCCAACCT	
gE	CCGAGGACGAGTTCAGCA	GGCCCATTCGTCACTTCCG	ACCAGACGTCGAAGCCGGA

Western blotting

To extract brain tissue and astrocyte proteins, the cells were lysed with RIPA lysis buffer supplemented with protease inhibitors. Proteins were quantified using the bicinchoninic acid (BCA) method. Following the standard western blotting protocol, rabbit primary antibodies against MMP-9, ZO-1, occludin, and collagen V and goat anti-rabbit antibodies (Table 2) were diluted and added to the samples. The expression levels of the target protein were calculated using the ratio of the grey value of the target protein band to the grey value of the β-actin band.

Immunofluorescence colocalization

Brain tissues fixed with paraformaldehyde were sectioned using a freezing microtome, deparaffinized in water, antigen repaired, inactivated with a hydrogen peroxide solution, blocked with serum, and incubated with antibodies against GFAP, CD31, and NueN (Table 2). The cells were incubated at room temperature for 1 h and repaired with CY3-TSA and trypsin (1%) for 8 min. Primary antibodies against MMP-9 were added, and the samples were incubated at 25 ℃ for 1 h. The cell nuclei were counterstained with DAPI, and the slides were blocked with an autofluorescence quencher, observed under a fluorescence microscope, and photographed (EVOS FL, Thermo Fisher, USA). ImageJ Fiji (National Institutes of Health, USA) digital pathology image analysis software was used for the analysis.

Morphological analysis of astrocytes

ImageJ software combined with NeuronJ and Sholl analysis plug-ins (National Institutes of Health, USA) was used to trace the branch lengths of astrocytes, and end-branch voxels were quantified.

Construction of a double-layer transwell model in vitro

Millicell hanging cell culture inserts with a pore size of 0.4 μm (Corning, USA) were placed into the wells of 12-well plates. C8-D1A (5×10^4/cm^2) cells were seeded on top of the transwell inserts and incubated at 37 °C. The chambers with C8-D1A cells were carefully transferred to new 12-well plates containing bEnd.3 cells (1×10^5/cm^2). A volume of 1.5 mL of DMEM plus 10% FBS was added to the bottom (basal) wells of the companion plate and incubated for 24 h at 37 °C in 5% CO_2.

Single-cell sequencing

A single-cell suspension (700–1200 cells/μL) was obtained by digestion of mouse brain tissue. The single-cell RNA-seq library of mouse brain tissue was established by amplification of the cell suspension into cDNA containing a barcode tag and UMI information. Sequencing was performed using an Illumina NovaSeq 6000

sequencing platform. CellRanger software (version 7.0.0) of the 10×Genomics platform was used for preliminary processing of single-cell transcriptome sequencing data to generate gene expression matrices, and R software (version 4.1.2) was used for reading and processing the genome and transcriptome data. The number of nFeature genes in the original data >200 and the proportion of mitochondrial UMI ≤25% were used as the screening criteria, and the "log normalization" process was performed. The batch effect was removed by Harmony package (version 0.1.1). Cluster analysis and visualization were performed by the FindClusters function to identify different cell clusters in the liver. The Wilcoxon rank sum test was performed with $P<0.05$ and |avg_log ″c|>0.25 as the data parameters, and DEGs were screened by FndMarkers function.

In vitro BBB permeability assays

A Millicell ERS-2 V-ohm meter (Millipore, Boston, MA, USA) was used to calculate trans-epithelial electrical resistance (TEER) by subtracting the resistance of the blank inserts from that of the inserts containing cells and multiplying the subtracted values by the area of the insert.

To determine the integrity of the in vitro BBB, a FITC-dextran permeability assay was conducted as described previously [18]. Briefly, after 3 days of culture, 40-kDa FITC-dextran (Sigma, 100 μg/mL) was added to the upper chamber of the transwell inserts. After 1 h, the medium in the lower chamber was collected and subjected to fluorescence analysis. A bare transwell insert under the same conditions was used as a mock control.

Transcriptome sequencing data processing

Total RNA was extracted using the TRIzol method and assessed for integrity with a Qsep400 bioanalyzer. mRNA was enriched using magnetic beads conjugated to oligo (dT), and RNA was fragmented into short pieces using a fragmentation buffer. First-strand cDNA synthesis was performed with a random hexamer primer and reverse transcriptase, followed by second-strand cDNA synthesis using the first strand as a template. The cDNA library was amplified via PCR and validated for insert size using a high-throughput nucleic acid protein analysis system. Sequencing was conducted on the Illumina platform, and the raw data were processed with fastp v0.23.2. Clean reads were aligned to the reference genome using HISAT2 v2.2.1.

Statistical analyses

Data normality was assessed using the Shapiro–Wilk test. Nonparametric comparisons among multiple groups were conducted using Kruskal–Wallis one-way ANOVA, followed by Holm's step-down Bonferroni method for p value adjustment. The Mann–Whitney U test was employed for pairwise comparisons. Normally distributed data were analysed by one-way ANOVA with Dunnett's or Tukey's post hoc test for multiple comparisons, as detailed in the figure legends. Significance was set at $p<0.05$. Statistical analyses were performed using Prism 10.2.3 software (GraphPad, La Jolla, CA, USA). The volcano map and KEGG bubble map were visualized by Rggplot2 (version 3.5.1). The enriched pathway network map was analysed by Metascape [19].

Results

Infection with PRV leads to neurological symptoms and induces brain damage in mice

To determine whether PRV infection causes neurological symptoms in mice, we replicated natural infection conditions, administered PRV nasally to the mice, and recorded their clinical symptoms and pathological changes. Our findings indicated that the mice began to exhibit cold aversion at 24 h, followed by dishevel and arched fur, as well as symptoms such as shortness of breath, shivering, lethargy, and ocular and nasal bleeding. All the mice died within 80 h after infection. In the 48-h group, mouse brain tissues exhibited signs of meningeal congestion and oedema. In the 72-h group, mouse brain tissues presented significant congestion and oedema, whereas the meninges presented prominent blood filaments. To further examine the pathological changes in the brain tissues, we conducted H&E staining of the brain tissues from each group. Pathological examination revealed that, compared with those in the control group, the number of visible Nissl bodies decreased in the 24-h group, and a small number of eosinophilic inclusions and lymphocytes were observed. In the 48-h group, nerve cells were lysed and formed cavities. Additionally, the neurons were lysed, which contributed to the formation of these cavities. The 72-h group presented normal Nissl bodies with no visible eosinophilic inclusions. Many neurons dissolve after the formation of cavities, accompanied by a phenomenon resembling "perivascular cuffing" (Figure 1A).

To further evaluate the effects of PRV in mice, we visually assessed the degree of nerve function damage following nerve injury. The mNSSs revealed that PRV impaired the neurological function of the mice in a time-dependent manner. Compared with those of the control group, the mNSSs of the 24 h group were not significantly different ($P>0.05$), whereas those of the 48 h and 72 h groups were significantly different ($P<0.01$) (Figure 1C).

To further investigate the changes in the viral load in the brain tissues of mice after PRV infection, samples of mouse brain tissues were obtained, and the viral load

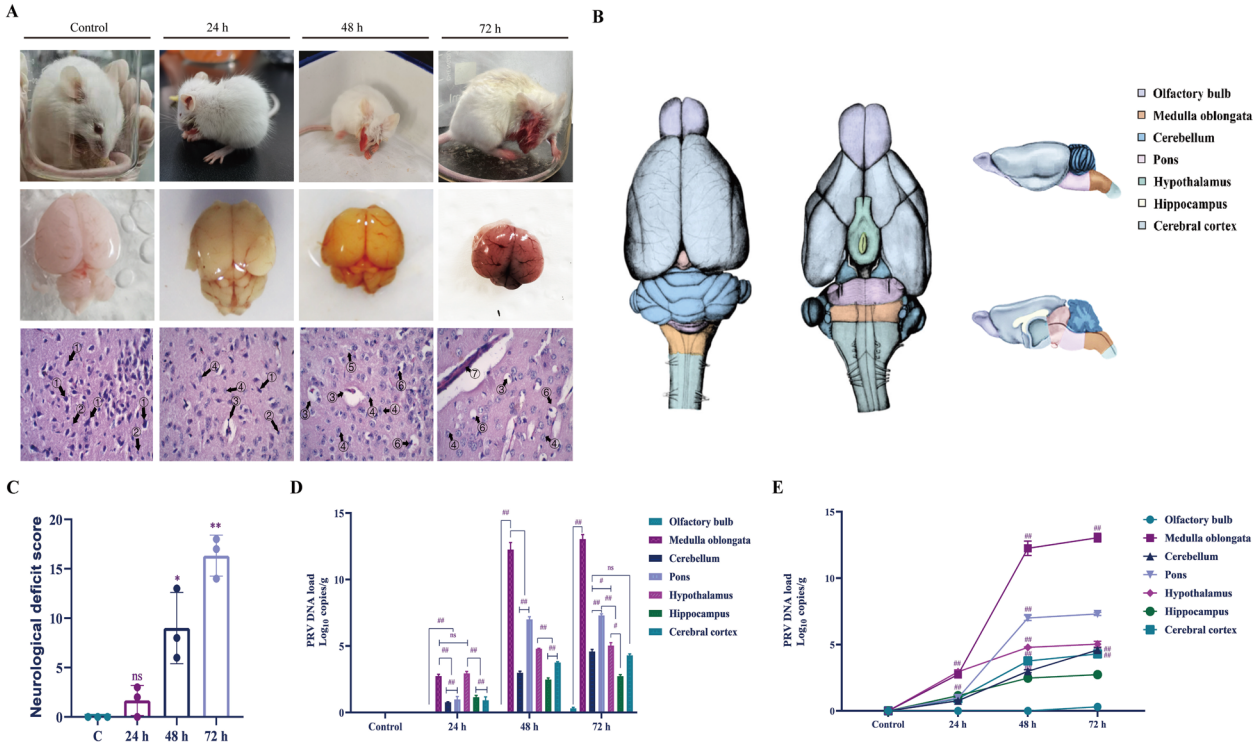

Figure 1 PRV infection leads to neurological symptoms and induces brain damage in mice. **A** Clinical symptoms (top), brain tissue images (middle), and H&E-stained sections (bottom) of the mice at different time points. **B** Schematic representation of brain tissue partitions in mice. **C** Neurological function score. **D** Bar graph of the PRV load in different brain tissue partitions at each time point. **E** Line plot of the PRV load in different brain tissue partitions at each time point. Note: There were 12 mice in each group. H&E staining (400×): ① Nissl bodies; ② microglia; ③ eosinophilic inclusion bodies; ④ lymphocytes; ⑤ nerve cell lysis; ⑥ neurons dissolving and forming cavities; and ⑦ vascular sheath. $P < 0.05$ was considered a significant difference, and $P < 0.01$ was considered a very significant difference. The difference between the Con group and the other groups is represented by *, and the difference within the other groups is represented by #.

of PRV was measured at different time points (Fig. 1B). These results indicate that PRV infection has a time-dependent relationship with the PRV load in the brains of mice. Specifically, the viral load increased with increasing duration of infection. At 24 h, the viral load was significantly greater in the medulla oblongata and hippocampus than in the other regions ($P < 0.01$). However, no virus was detected in the olfactory bulb. After the 48-h and 72-h infection periods, the viral load in the medulla oblongata peaked, significantly surpassing that in other regions of the brain ($P < 0.01$). PRV was detected in all regions at 72 h; however, the viral load in the olfactory bulb was not significantly different from that in the control group ($P \geq 0.05$) (Fig. 1E). Compared with those of the control group, except for those in the olfactory bulb, the viral loads in the brain regions of the 24-h group were extremely significantly different ($P < 0.01$); compared with those at 24 h, the viral loads in the brain regions of the 48-h group were significantly different ($P < 0.01$). Compared with those in the 48-h group, the viral loads in the medulla oblongata, cerebellum, and hippocampus were significantly different ($P < 0.01$) (Fig. 1F). In summary, PRV induces viral encephalitis and neurological damage in mice.

PRV can penetrate the BBB and disrupt tight junctions (TJs)

To further explore the influence of PRV on the BBB, we conducted transmission electron microscope imaging of brain tissues. An increase in the separation of TJs in membranes is a marker of TJ dysfunction [11]. In the 48-h and 72-h groups, a significant increase in the distance between TJs in the membranes was observed, indicating damage to the BBB (Fig. 2A).

To further assess the integrity of the BBB, the concentration of Evans blue and the water content in mouse brain tissues were quantified. Evans blue staining is widely used to assess BBB permeability and brain tissue damage [20].

The brain tissue water content is an important indicator for assessing the severity of brain oedema [21]. After PRV attack, the W/D value of mouse brain tissues increased. Furthermore, the W/D value continued to increase with increasing infection duration. Significant differences were observed in the W/D values

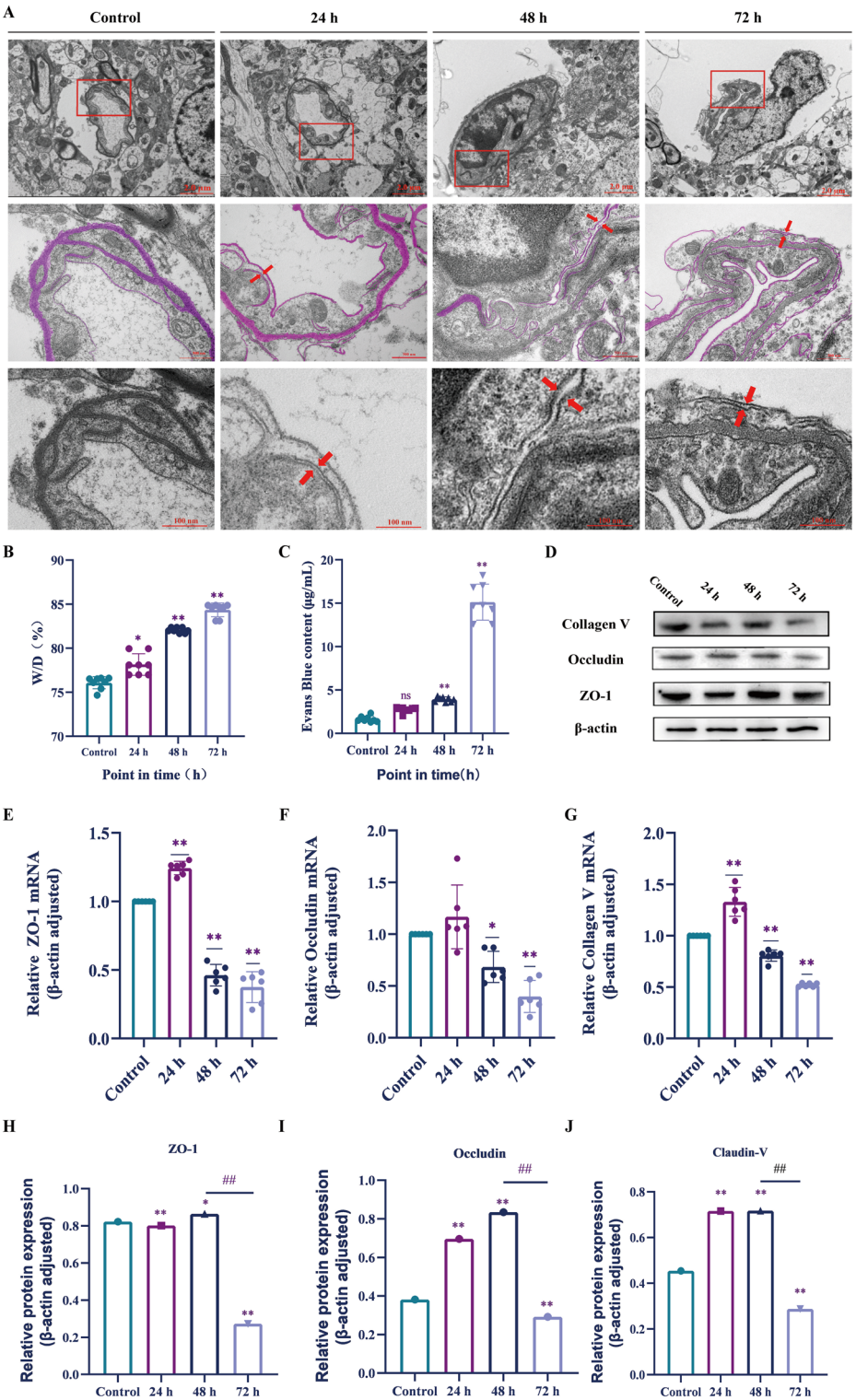

Figure 2 PRV can penetrate the BBB and disrupt tight junctions (TJs). **A** TEM images of the tight junction. **B** W/D values of mouse brain tissue after PRV challenge. **C** Evans blue concentration of mouse brain tissue after PRV challenge. **D** Protein bands of MMP-9, ZO-1, collagen V, occludin and β-actin. **E** mRNA expression levels of ZO-1. **F** mRNA expression levels of occludin. **G** mRNA expression levels of collagen V. **H** ZO-1 staining was measured by ImageJ software. **I** occludin staining was measured by ImageJ software. **J** collagen V staining was measured by ImageJ software. Note: There were 12 mice in each group. $P < 0.05$ was considered a significant difference, and $P < 0.01$ was considered a very significant difference. The difference between the Con group and the other groups is represented by *, and the difference within the other groups is represented by #.

of the 24-h group compared with those of the control group ($0.01 \leq P < 0.05$), and those of the 48-h and 72-h groups were extremely significantly different ($P < 0.01$) (Fig. 2B). Changes in the concentration of Evans blue in mouse brain tissues following PRV challenge were time dependent. Compared with that in the control group, there was no significant difference in the Evans blue concentration in the 24-h group ($P < 0.05$), but the concentrations in the 48-h and 72-h groups were significantly different ($P < 0.01$) (Fig. 2C).

Additionally, we analysed the mRNA and protein expression levels of the tight junction proteins ZO-1, occludin, and collagen V. Compared with those in the control group, the mRNA expression levels of ZO-1, occludin, and collagen V initially increased but then decreased, with the highest levels observed in the 24-h group and the lowest levels observed in the 72-h group ($0.01 \leq P < 0.05$) (Figures 2E–G). The protein expression of ZO-1, occludin, and collagen V initially increased but then decreased, with the highest and lowest levels observed in the 24-h group and 72-h group, respectively (Figures 2H–J). In conclusion, these findings suggest that PRV affects the host by damaging TJ integrity in the BBB.

MMP-9 mediates collagen VI degradation and BBB disruption

Studies have reported that the MMP-9-mediated degradation of collagen IV contributes to the disruption of the BBB in viral encephalopathy [22]. However, the substrate underlying PRV-induced BBB disruption is unclear. Through the correlation between the differentially expressed genes and terms, we found that the differentially expressed gene Col6a6 could regulate the ECM-receptor interaction pathway (Fig. 3B). We hypothesized a potential interaction between MMP-9 and collagen VI, which was investigated by molecular docking and coimmunoprecipitation assays. The findings confirmed a direct interaction between these proteins, with elevated MMP-9 levels inducing collagen VI degradation ($P < 0.01$) (Figures 3C–D). These findings indicate that MMP-9 is a critical mediator of PRV-induced BBB disruption.

PRV infection increases astrocyte proliferation, promoting A1 subtype transition

To elucidate the cellular mechanisms underlying PRV-induced viral encephalopathy in mice, we conducted single-cell RNA sequencing on brain tissues before and after PRV infection. The analysis revealed a significant increase in the number of astrocytes following PRV infection (Figures 4A, B). Further characterization of astrocyte subtypes revealed a transition from the A2 phenotype to the A1 phenotype post-infection (Figures 4C, D). To further validate this idea, we utilized ImageJ software (National Institute of Health) in combination with the Neuron J and Sholl analysis plugins to track and analyse the reactivity of astrocytes at different time points following PRV infection. Reactive astrocytes labelled with GFAP were mapped on the basis of their outlines and tracing patterns (Fig. 4E). With increasing virus challenge time, there was a significant decrease in the number of endpoint voxels of astrocytes ($P < 0.01$) (Fig. 4F). The branch length (Fig. 4G) and maximum branch length significantly increased ($P < 0.01$) (Fig. 4H). These findings indicated that reactive astrocytes gradually transitioned to the A1 type following PRV infection.

Astrocytes primarily produce MMP-9

Astrocytes can secrete MMP-9, which can exacerbate damage to the BBB under pathological conditions, such as trauma [23] and ischemic brain injury [24]. However, whether astrocytes are the primary source of MMP-9 after PRV infection remains unclear. Therefore, we utilized colocalization to determine the site of viral invasion at 72 h post infection using GFAP/MMP-9, neuronal nuclei (NeuN)/MMP-9, and CD31/MMP-9. The Pearson coefficients between GFAP and MMP-9, NeuN and MMP-9, and the endothelial cell adhesion molecules CD31 and MMP-9 were 0.897, 0.121, and 0.612, respectively. Simultaneously, the intensity/distance figure indicated a nearly unanimous change in the strength of MMP-9 and GFAP expression, which had little overlap with NeuN, per half of the change in CD31 expression (Figures 5A–C). These findings indicate that MMP-9 is derived primarily from astrocytes, with a small amount derived from endothelial cells.

To further confirm the increase in astrocyte secretion of MMP-9 over time during viral invasion, the colocalization of GFAP and MMP-9 was subsequently examined at different time points (Fig. 5D). These findings indicate a positive correlation between the secretion of MMP-9 by astrocytes and the duration of PRV challenge. Specifically, as the duration of viral infection increased, the secretion of MMP-9 by astrocytes increased. Compared with that in the control group, there was a significant increase in the expression of MMP-9 in the 48-h and 72-h groups ($P < 0.01$) (Fig. 5E).

PRV enters the BBB paracellularly, with MMP-9 deletion reversing damage

Three distinct mechanisms for crossing the BBB have evolved for blood-borne virus pathogens: transcellular, paracellular, and “Trojan horse” entry. To determine

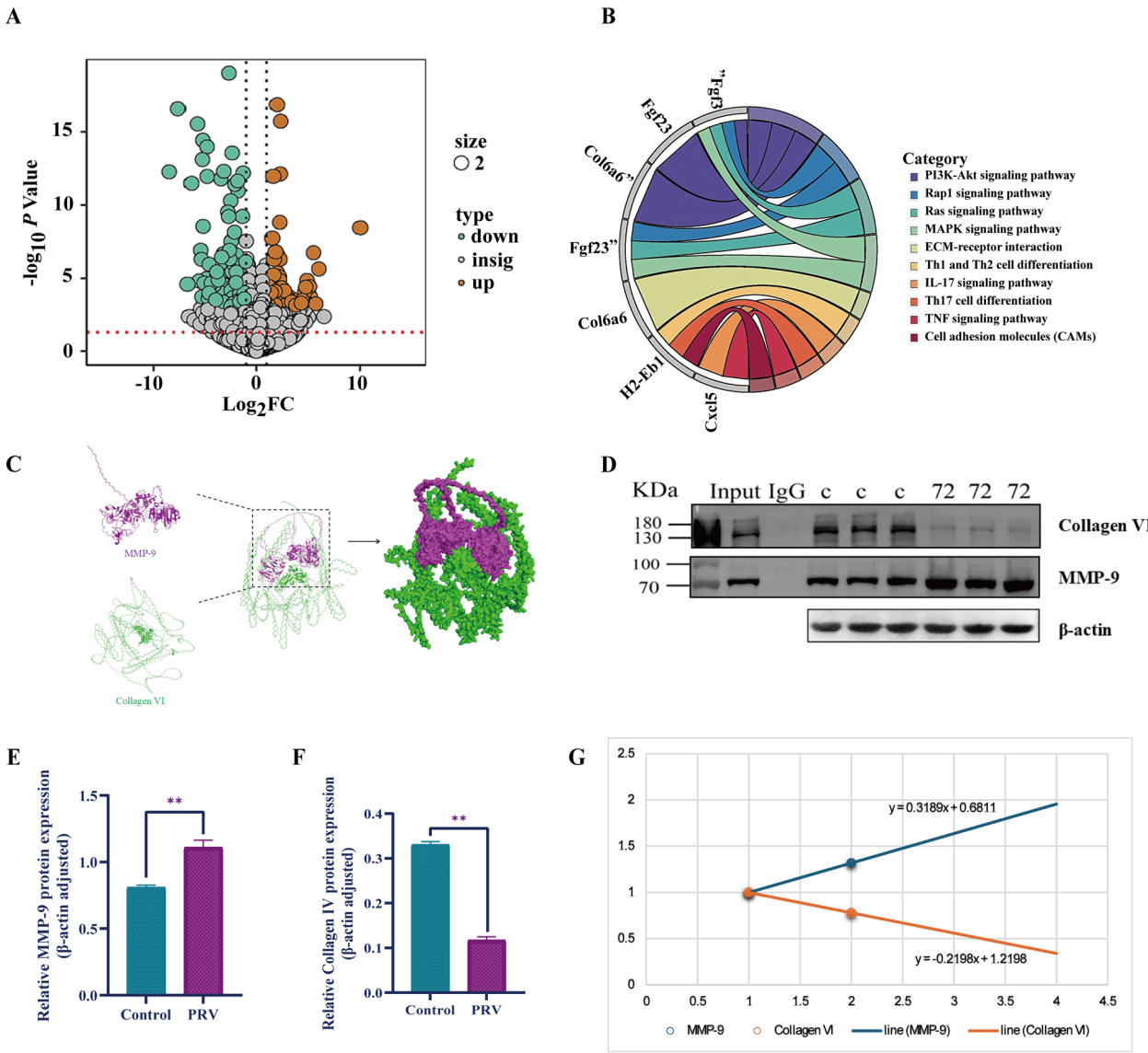

Figure 3 MMP-9 mediates collagen VI degradation and BBB disruption. **A** Volcano map of differentially expressed genes between PRV and normal brain tissue samples ($log_2FC|> 1$, daily P value < 0.05). **B** Chord diagram of gene function. **C** Molecular docking of MMP-9 and collagen VI. **D** Co-IP of MMP-9 and collagen VI. **E** MMP-9 staining was measured by ImageJ software. **F** Collagen VI staining was measured by ImageJ software. **G** Correlation analysis of MMP-9 and collagen VI. Note: Six mice were grouped for transcriptome analysis. $P < 0.05$ was considered a significant difference, and $P < 0.01$ was considered a very significant difference. The difference between the Con group and the other groups is represented by *, and the difference within the other groups is represented by #.

the mechanism underlying PRV penetration of the BBB, we established a double transwell in vitro model of the BBB (Fig. 6A). Immunofluorescence (IF) revealed that this model comprised endothelial cells and astrocytes (Fig. 6B). Using FITC-conjugated dextran (40 kDa) and measuring TEERs, we evaluated our model's function and electrophysiology of transwell BBB permeability. Compared with the control group, the transwell BBB model was successfully established (Figures 6D–E). The viral load at different time points in the transwell BBB model. The variations in the lower chamber viral load were time dependent. Compared with those of the control group, the viral loads of the infection groups were extremely significantly different ($P < 0.01$) (Fig. 6C), indicating that PRV can pass through the BBB. The results from the FITC-conjugated dextran experiment suggested that the exudation of FITC-dextran was most pronounced in the 24-h group, and this difference was highly significant

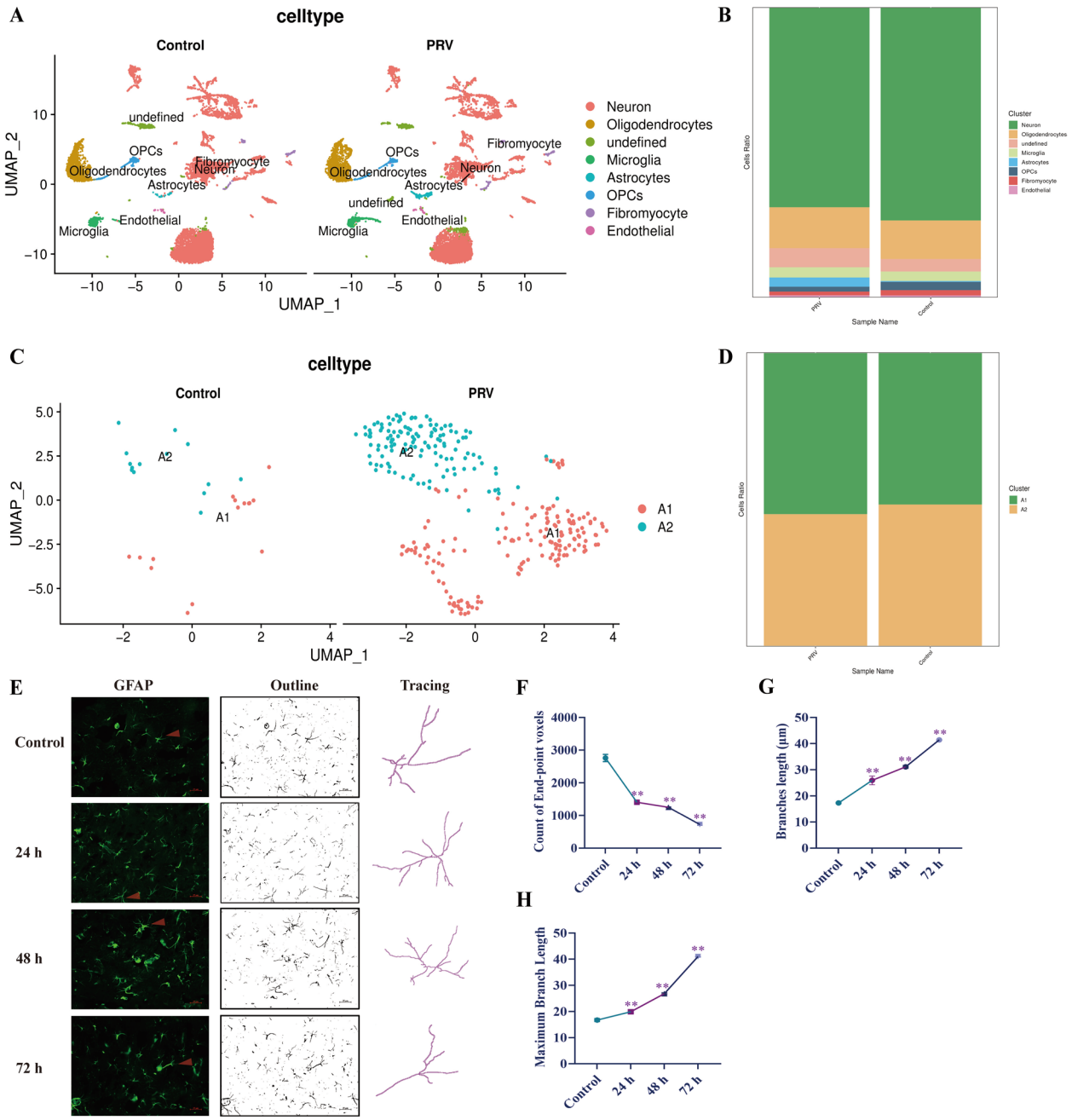

Figure 4 PRV infection increases astrocyte proliferation, promoting A1 subtype transition. **A** UMAP visualizes the cellular component map. **B** Cell proportion diagram. **C** UMAP visualizes the astrocyte's cellular component map. **D** A1 and A2 astrocyte proportion diagram. **E** PRV infection of mouse brain astrocytes at different time points after immune marker analysis and morphological analysis. **F** End-point voxel analysis of astrocytes. **G** Branches length of the astrocytes. **H** Maximum branch length of the astrocytes. Note: Three mice per group were used for single-cell sequencing. $P < 0.05$ was considered a significant difference, and $P < 0.01$ was considered a very significant difference. The difference between the Con group and the other groups is represented by *, and the difference within the other groups is represented by #.

compared with that in the control group ($P < 0.01$) (Fig. 6D). In addition, the lowest TEER occurred in the 24-h group, which was significantly different from that in the 12-h and 24-h groups ($P < 0.01$) (Fig. 6E). These findings suggest that PRV enhances BBB permeability.

To further elucidate whether PRV permeates the BBB via a para-cellular pathway, the mRNA and protein

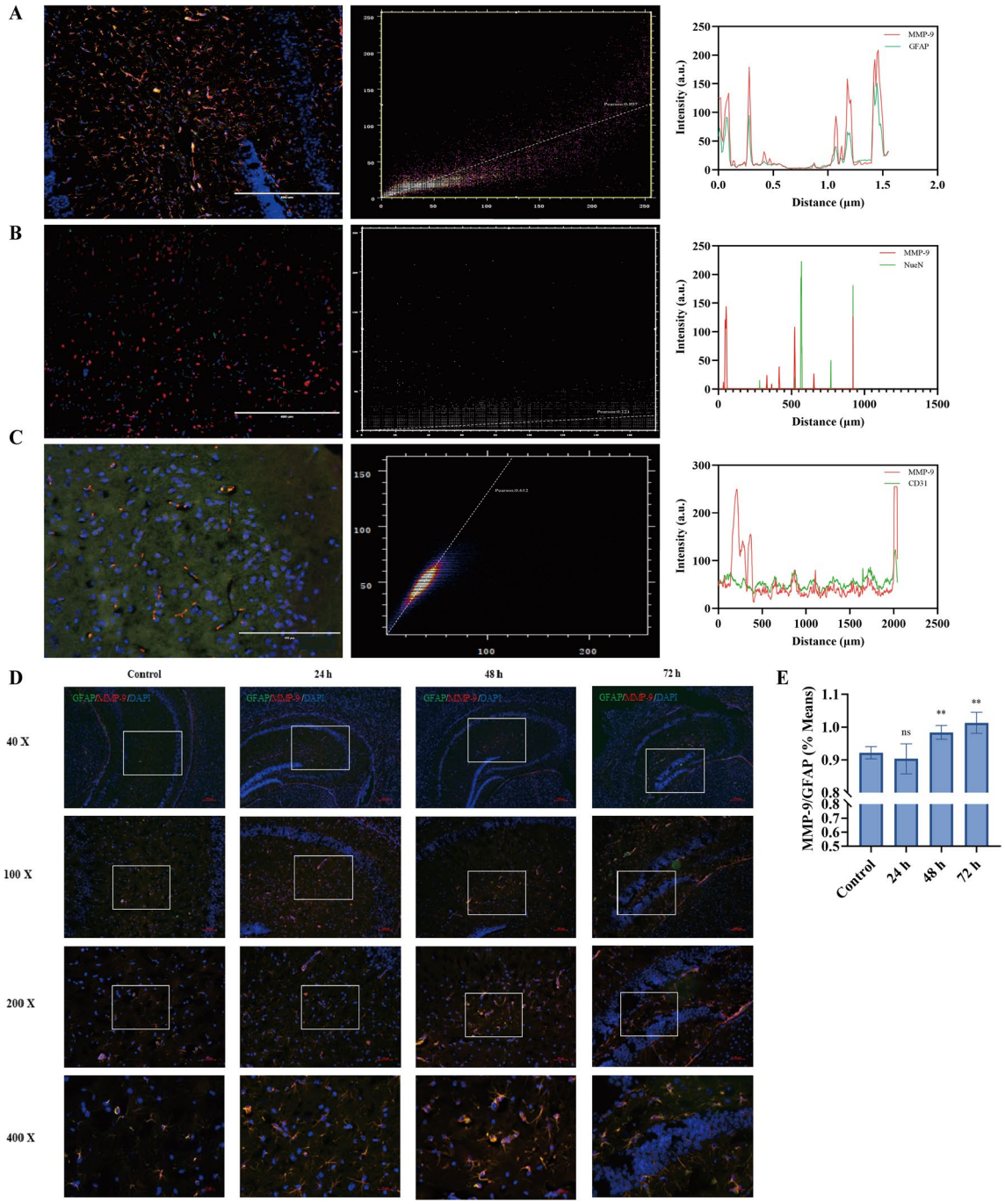

Figure 5 Astrocytes primarily produce MMP-9. A Colocalization of MMP-9 and GFAP at 72 h (200X) (Left); Pearson index analysis of MMP-9 and GFAP at 72 h (Middle); Intensity/Distance analysis of MMP-9 and GFAP at 72 h (Right). **B** Colocalization of MMP-9 and NeuN at 72 h (200X) (Left); Pearson index analysis of MMP-9 and NeuN at 72 h (Middle); Intensity/Distance analysis of MMP-9 and NeuN at 72 h (Right). **C** Colocalization of MMP-9 and CD31 at 72 h (200X) (Left); Pearson index analysis of MMP-9 and CD31 at 72 h (Middle); Intensity/Distance analysis of MMP-9 and CD31 at 72 h (Right). **D** Fluorescence colocalization map of GFAP and MMP-9 at different time points. **E** Quantitative analysis of GFAP and MMP-9 fluorescence intensity at different time points. Note: There were 3 mice in each group. $P < 0.05$ was considered to indicate a significant difference, $P < 0.01$ was considered to indicate a very significant difference. The difference between the Con group and the other groups is represented by *, and the difference within the other groups is represented by #.

expression levels of occludin, ZO-1, and collagen V were examined. The results of real-time PCR revealed a significant decrease in the mRNA levels of ZO-1, collagen V, and occludin at various time points compared with those in the control group ($P < 0.01$) (Figures 6G–I). The WB results revealed that, compared with that in the control group, the expression of 3 tight junction proteins decreased first but then increased and reached the lowest value at 24 h ($P < 0.01$). Except for ZO-1, there was no significant difference in occludin or collagen V protein expression between the 24 and 48 h groups ($P \geq 0.05$) (Figures 6F, J–L). These data indicate that PRV accesses the BBB via the paracellular pathway, disrupting tight junctions during this process.

To ascertain the link between TJ disruption and MMP-9 expression, we ablated the MMP-9 gene (Fig. 6N). The results indicated that MMP-9 deletion mitigated TJ damage upon subsequent PRV infection (Figures 6O–R), suggesting that MMP-9 is a critical gene that exacerbates BBB injury during PRV infection.

PRV invades the CNS and causes an "inflammatory storm"

An inflammatory storm, also known as a cytokine storm, is an overreaction of the immune system in which immune cells release large amounts of cytokines, leading to an uncontrolled inflammatory process. Following viral infection, there may be subsequent onset of viral encephalitis, leading to an "inflammatory storm". Therefore, we measured the levels of the chemokines CCL-3, CCL-4, and CCL-5; the cytokines IL-6 and IL-18; and TNF-α and INF-γ. The results indicated that the expression of all factors except INF-γ increased following PRV infection and peaked at 48 h. The expression of these factors significantly differed from that in the control group ($P < 0.01$) (Figures 7A–E, G). Compared with that in the control group, there was a significant decrease in INF-γ expression ($P < 0.01$) (Fig. 7F).

Discussion

PRV is a typical neurotropic virus [25] with an extremely wide range of secondary hosts, and it can infect most mammals, including humans [3]. PRV infection in newborn piglets is often acute and fatal, resulting in neurological symptoms. The mortality rate is close to 100%, which results in significant economic losses to the swine industry [26, 27]. In secondary hosts, PRV infection can lead to neurological symptoms such as itching, tremors, and ataxia. It can also cause nerve inflammation and result in death [28, 29]. However, the mechanism of invasion of PRV into the CNS via the BBB remains unclear.

PRV can be transmitted upwards through the olfactory, trigeminal, sympathetic, parasympathetic, or facial nerve pathways following intranasal infection in animals [25, 30]. In the initial phase of this study, we found that the viral infection route was through the olfactory bulb, brain, cerebellum, and brainstem. By extension, PRV propagates retrogradely through the nasal mucosa to the olfactory nerve, where it replicates. It then reaches other regions of the cerebrum through the neuronal axon, followed by the cerebellum, pons, and medulla oblongata, where high viral replication occurs, resulting in dyskinesia and respiratory failure in pigs [6]. In this study, viral particles were not observed in the olfactory bulb within 48 h following intranasal PRV infection in mice. At 72 h post-infection, the viral load in the olfactory bulb was low. However, compared with that in the control group, the viral load was not significantly different ($P > 0.05$). These findings suggest that PRV does not spread in a retrograde manner to the CNS through the olfactory pathway in mice. In contrast, in pigs, PRV is transmitted mainly upwards through the olfactory and trigeminal nerves, probably because the olfactory nerve terminals in pigs express receptors for PRV. Studies have shown that the glycoproteins of PRV play crucial roles in the infection and spread of the virus. Mutations in the viral envelope proteins gB, gC and gD can increase the ability of PRV to invade nerve cells. In particular, mutations in the gD protein significantly increase the affinity of PRV for the host receptor [31, 32]. This difference in affinity may be one of the reasons why PRV is more easily transmitted in pigs. Olfactory bulb cells in mice may not express or express fewer PRV receptors, whereas porcine olfactory bulb cells may express more PRV receptors, allowing the virus to spread and replicate more easily in the porcine olfactory bulb [33]. The spread of PRV also involves its neurotropism. Variants of PRV exhibit greater neurotropism, which is associated with mutations in viral envelope proteins that increase the ability of the virus to invade nerve cells. The strain we used, PRV-QJ, is affiliated with the Ea strain according to a nucleotide phylogenetic tree [34]. However, previous experiments revealed that the gD glycoprotein of the Ea strain and the classical Fa strain varies [35]. Therefore, we speculate that the difference in infectivity is related to the variation in the viral gD glycoprotein and the variation in the PRV virion.

The BBB plays a crucial role in establishing and maintaining the stability of the microenvironment within the CNS. It serves as an important barrier that is closely connected to functionality. TJs and transport proteins prevent the invasion of neurotropic pathogens and other substances [36, 37]. The separation of membranes at tight junctions is reportedly indicative of TJ dysfunction [38]. Our results revealed that the gap significantly widened at 48 and 72 h, indicating that the integrity of the BBB was disrupted. Additionally, in our animal experiments, decreased collagen V, occludin, and ZO-1 expression was

observed, which further supported these findings. However, these observations in animals do not provide insight into the molecular mechanism involved. Our in vivo experiments revealed decreased expression of TJ proteins after PRV infection in mice, confirming that BBB integrity is impaired; however, the mechanism underlying the passage of PRV through the BBB remains unclear.

To further investigate the mechanisms underlying the permeation of PRV through the BBB, we constructed a two-layer transwell model to simulate the BBB. Several neurotropic pathogens have evolved to use one of three mechanisms to cross the BBB. The first is transcellular entry, in which viruses, such as West Nile virus, Zika virus and Japanese encephalitis virus (JEV), pass through infected endothelial cells. The second route is pacellular entry, in which viruses, including Marburg virus, dengue virus and Ebola virus, enter by destroying TJ proteins, the actin cytoskeleton, or the basal lamina. The third route is "Trojan horse" entry, in which viruses, including human immunodeficiency virus, JEV, measles virus and canine distemper virus, infect leukocytes of the peripheral immune system and carry the virus into the CNS [39]. Viruses have different routes of entry into the CNS through the BBB, which may be related to their respective biological properties, interactions with the host, mechanisms of immune escape, and direct effects on endothelial cells. In future studies, the reasons for the different pathways of entry of different pathogens into the BBB can be further explored from the above aspects.

Transcellular entry is independent of TJ proteins, the actin cytoskeleton, and basement membrane disruption [40], whereas cellular entry relies on the regulation of TJ proteins between endothelial cells [41]. The "Trojan horse" approach relies on the peripheral white blood cells of the immune system [8, 42]. We observed that PRV infection led to an increase in the permeability of the BBB model, as indicated by an increase in FITC-conjugated dextran and a decrease in the TEER value. Additionally, the expression levels of TJ proteins (collagen V, occludin and ZO-1) confirmed that PRV can enter the CNS via the paracellular route by crossing the BBB.

Astrocytes respond to various CNS injuries by forming reactive astrocytes that are pathological hallmarks of structural lesions in the CNS [43]. Reactive astrocytes can be classified into two phenotypes on the basis of differences in gene expression: types A1 and A2. These phenotypes are functionally neurotoxic and neuroprotective, respectively [44]. Compared with A2-type astrocytes, reactive astrocytes of the A1 phenotype present fewer synapses, longer branches, and decreased functional strength [45]. Our results revealed that the number of astrocytes increased and that the phenotype changed from A2 to A1 after PRV infection. This may be related to the ability of astrocytes to respond to inflammatory signals. Studies have shown that astrocytes respond to inflammatory signals through signal transduction pathways, such as the NF-kB and JAK/STAT pathways. NF-κB and STAT3, as transcription factors, play key roles in initiating the expression of genes related to astrogliosis [46, 47]. In neurodegenerative diseases, such as Alzheimer's disease, Parkinson's disease and amyotrophic lateral sclerosis, astrocyte proliferation can drive disease progression [48]. Many inflammatory pathways, such as Th1 and Th2 cell differentiation, the IL-17 signalling pathway, Th17 cell differentiation and the TNF signalling pathway, were also enriched in our transcriptome results. The enrichment of these pathways led us to speculate about the relationship between astrocyte type and neuroinflammation. Subsequent experiments could be performed from this perspective.

Notably, the IL-17 signalling pathway was enriched in the transcriptome analysis. In the current research on PRV, the TLR4-MyD88-NF-κB pathway and inflammasome pathway were shown to be involved almost exclusively. However, from the KEGG website, only the nf-kappa B pathway is in the middle of a channel. Our study preliminarily explored the level of the PRV-related pathway and verified the downstream factor MMP-9 that regulates this pathway. These findings provide new targets for the subsequent search for drugs to treat PRV.

The significance of the inflammatory storm is particularly important in the context of viral encephalitis [49]. Viral encephalitis is an inflammatory disease caused by direct virus invasion of the central nervous system and is characterized by inflammation of the brain parenchyma. When an inflammatory storm occurs, immune cells within the central nervous system, such as microglia and astrocytes, are activated, releasing large amounts of cytokines such as TNF-α, interleukins, and IFNs. Excessive production of these cytokines can exacerbate inflammatory damage to brain tissue, leading to blood–brain barrier disruption, neuronal damage and dysfunction [49–51]. Determination of the expression of the cytokines IL-6 and IL-18 and TNF-α and INF-γ revealed a decrease in INF-γ levels. INF-γ is not only a proinflammatory factor but also an antiviral factor. Our results indicate that PRV can evade the host's innate immune response by blocking INF-γ production. These findings indicate the need for further studies on PRV immune escape mechanisms and the development of new strategies against viral infections. Chemokines are essential for immune cell adhesion to the vasculature. The "Trojan horse" approach relies on immune cells that infiltrate the CNS [42]. In this study, measurement of the expression levels of the chemokines CCL-3, CCL-4, and CCL-5 revealed an increase in chemokine expression. These

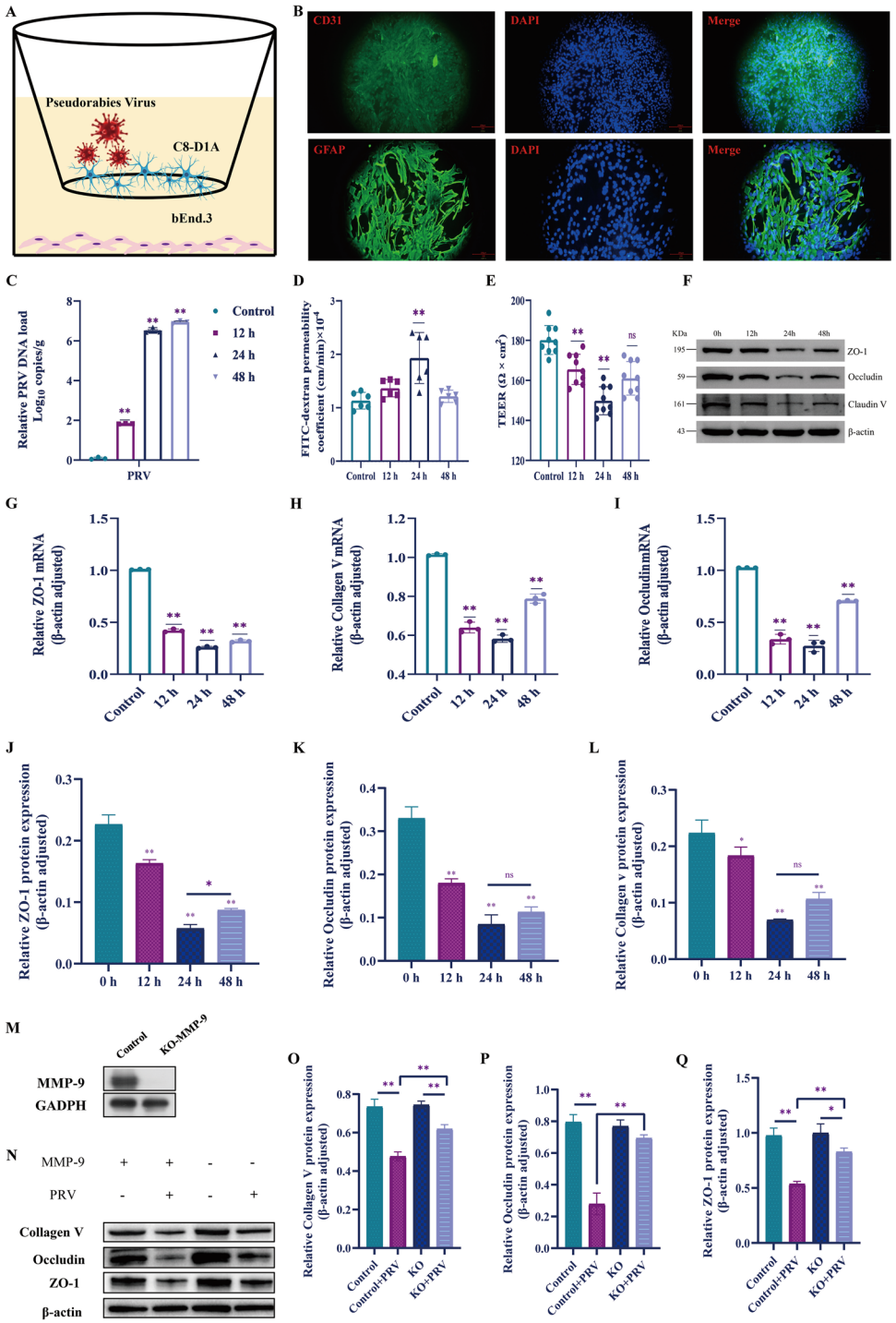

Figure 6 PRV enters the BBB paracellularly, with MMP-9 deletion reversing damage. A Schematics of the in vitro transwell BBB model. **B** An in vitro transwell BBB model was identified by IFC. **C** Viral load measurement of the transwell BBB model after PRV infection. **D** FITC-dextran concentrations at different time points. **E** TEER at different time points. **F** ZO-1, occludin, collagen V and β-actin protein bands. **G** mRNA expression levels of ZO-1. **H** mRNA expression levels of collagen V. **I** mRNA expression levels of occludin. **J** Z0—1 staining was measured by ImageJ software. **K** Occludin staining was measured by ImageJ software. **L** Collagen V staining was measured by ImageJ software. **M** Protein bands of WT and KO-MMP-9. **N** Protein bands of WT and KO-MMP-9 cells before and after PRV infection. **O** Collagen V staining was measured by ImageJ software (WT vs KO-MMP-9). **P** Occludin staining was measured by ImageJ software (WT vs KO-MMP-9). **Q** ZO-1 staining was measured by ImageJ software (WT vs KO-MMP-9). Note: $P < 0.05$ was considered a significant difference, and $P < 0.01$ was considered a very significant difference. The difference between the Con group and the other groups is represented by *, and the difference within the other groups is represented by #.

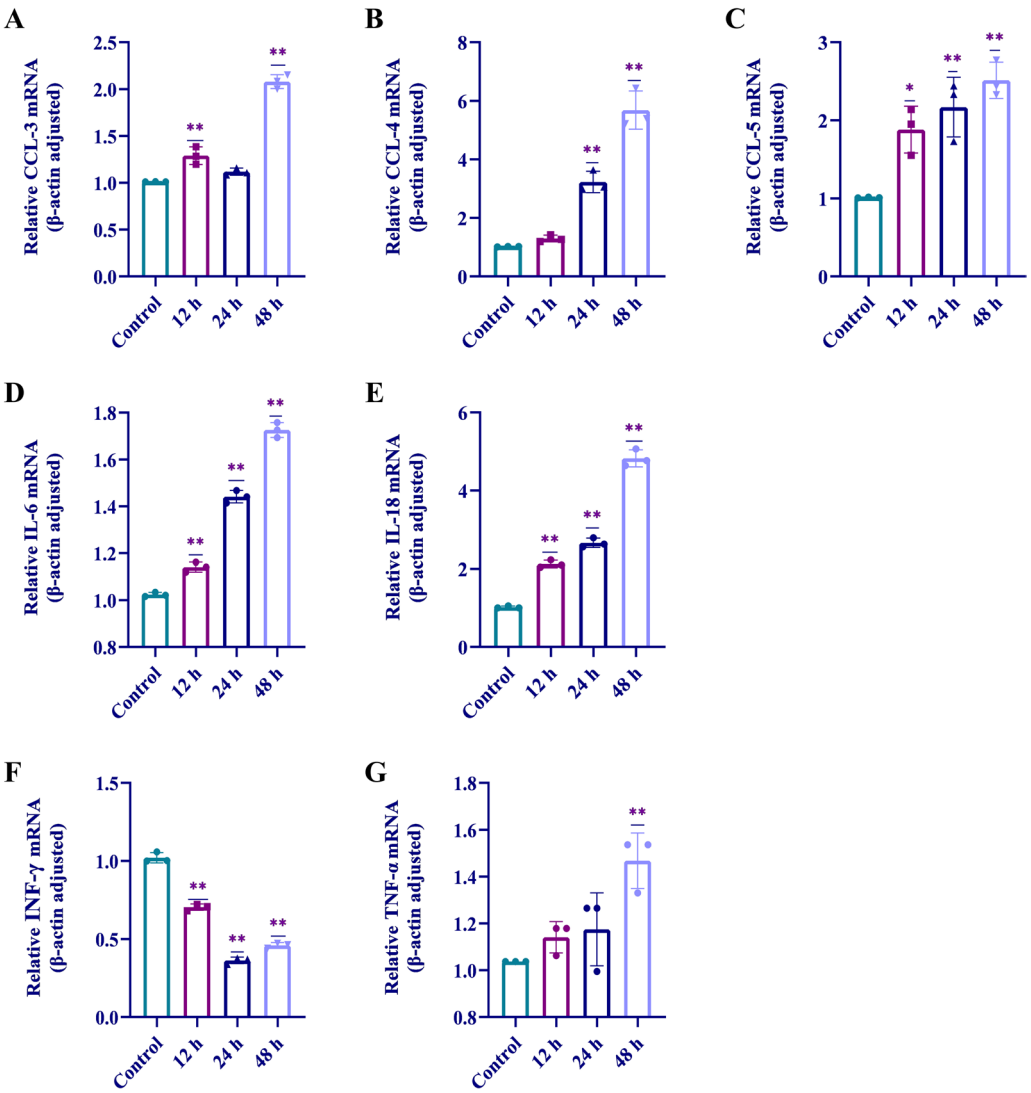

Figure 7 mRNA levels of inflammatory factors at different time points after PRV infection. **A** mRNA expression levels of CCL-3. **B** mRNA expression levels of CCL-4. **C** mRNA expression levels of CCL-5. **D** mRNA expression levels of IL-6. **E** mRNA expression levels of IL-18. **F** mRNA expression levels of INF-γ. **G** mRNA expression levels of TNF-α. $P < 0.05$ was considered a significant difference, and $P < 0.01$ was considered a very significant difference. The difference between the Con group and the other groups is represented by *, and the difference within the other groups is represented by #.

findings suggest that the invasion of the CNS by PRV may not depend on one pathway. This phenomenon has been observed in other viruses. For example, Japanese encephalitis virus utilizes transcellular [52] and Trojan horse entry [8] to cross the BBB. Moreover, SARS-CoV-2 is capable of transcellular [41] and paracellular entry [53] into the BBB.

In conclusion, our study provides compelling evidence that PRV infection in mice leads to a cascade of neurological symptoms and brain damage characterized by a time-dependent increase in the viral load within the brain, particularly in the medulla oblongata and hippocampus. The ability of a virus to penetrate the BBB is facilitated by its paracellular entry, which is associated with the disruption of tight junctions and a subsequent increase in BBB permeability. This disruption is mediated by MMP-9, which is produced primarily by astrocytes and contributes to the degradation of collagen VI, a key component of the BBB. Infection also triggers a significant increase in astrocyte proliferation and a shift towards the A1 astrocyte subtype, which is known to secrete high levels of MMP-9, further exacerbating BBB damage.

Acknowledgements
This study was supported by the National Natural Science Foundation of China (Grant 32360903). We are grateful for the strong support of the Yunnan Agricultural University of Pig Healthy Breeding Technology Innovation Team. We thank Professor Xing Liu from Nanjing Agricultural University for providing valuable and constructive feedback that significantly enhanced the manuscript. Thanks to Animal Husbandry and the Veterinary Academy of Sciences; in Yunnan Province, Jun Yao provided the PRV.

Authors' contributions
Ying Zhang: Writing—original draft; CS: Writing—review and editing; Ying Zhang: supervision; XS: conceptualization; YW: methodology; KC: data curation; XZ: writing—visualization; Yalong Sun: software; HS: data curation; QW: conceptualization; JL: formal analysis; Yue Shu: conceptualization. All authors read and approved the final manuscript.

Funding
This study was supported by the National Natural Science Foundation of China (Grant 32360903).

Availability of data and materials
The datasets used and/or analysed during the current study are available from the corresponding author upon reasonable request.

Declarations

Ethics approval and consent to participate
All experiments performed in this study were approved by the International Animal Care and Use Committee of Yunnan Agricultural University (permission code: 202405003; date of approval: January 1, 2022). This study complied with the guidelines of the Institutional Administration and Ethics Committee for Laboratory Animals.

Competing interests
The authors declare that they have no competing interests.

Received: 24 July 2024 Accepted: 17 January 2025
Published online: 02 April 2025

References

1. Bo Z, Li X (2022) A review of pseudorabies virus variants: genomics, vaccination, transmission, and zoonotic potential. Viruses 14:1003. https://doi.org/10.3390/v14051003
2. Zhou M, Abid M, Cao S, Zhu S (2023) Recombinant pseudorabies virus usage in vaccine development against swine infectious disease. Viruses 15:370. https://doi.org/10.3390/v15020370
3. Liu Q, Wang X, Xie C, Ding S, Yang H, Guo S, Li J, Qin L, Ban F, Wang D, Wang C, Feng L, Ma H, Wu B, Zhang L, Dong C, Xing L, Zhang J, Chen H, Yan R, Wang X, Li W (2022) Erratum to: a novel human acute encephalitis caused by pseudorabies virus variant strain. Clin Infect Dis 74:756. https://doi.org/10.1093/cid/ciab550
4. Wang H, Zeng L, Li W, Wang S (2022) Teaching NeuroImage: human encephalitis caused by pseudorabies virus infection. Neurology 99:311–312. https://doi.org/10.1212/WNL.0000000000200882
5. Ou J, Cai S, Zheng F, Lu G, Zhang G (2020) Human pseudorabies virus infection: a new threat in China. J Infect 80:578–606. https://doi.org/10.1016/j.jinf.2019.12.018
6. Song C, Huang X, Gao Y, Zhang X, Wang Y, Zhang Y, Lv T, Zhang Z, Zhang Y, Pan Q, Shu Y, Shu X (2021) Histopathology of brain functional areas in pigs infected by porcine pseudorabies virus. Res Vet Sci 141:203–211. https://doi.org/10.1016/j.rvsc.2021.10.011
7. Michinaga S, Koyama Y (2019) Dual roles of astrocyte-derived factors in regulation of blood-brain barrier function after brain damage. Int J Mol Sci 20:571. https://doi.org/10.3390/ijms20030571
8. Zou SS, Zou QC, Xiong WJ, Cui NY, Wang K, Liu HX, Lou WJ, Higazy D, Zhang YG, Cui M (2022) Corrigendum: brain microvascular endothelial cell-derived HMGB1 facilitates monocyte adhesion and transmigration to promote JEV neuroinvasion. Front Cell Infect Microbiol 12:964880. https://doi.org/10.3389/fcimb.2022.964880
9. Bassiouni W, Ali M, Schulz R (2021) Multifunctional intracellular matrix metalloproteinases: implications in disease. Febs J 288:7162–7182. https://doi.org/10.1111/febs.15701
10. Kurzepa J, Kurzepa J, Golab P, Czerska S, Bielewicz J (2014) The significance of matrix metalloproteinase (MMP)-2 and MMP-9 in the ischemic stroke. Int J Neurosci 124:707–716. https://doi.org/10.3109/00207454.2013.872102
11. Jackson RJ, Meltzer JC, Nguyen H, Commins C, Bennett RE, Hudry E, Hyman BT (2022) APOE4 derived from astrocytes leads to blood-brain barrier impairment. Brain 145:3582–3593. https://doi.org/10.1093/brain/awab478
12. Tao Y, Zhang L, Yang R, Yang Y, Jin H, Zhang X, Hu Q, He B, Shen Z, Chen P (2021) Corilagin ameliorates atherosclerosis by regulating MMP-1, -2, and -9 expression in vitro and in vivo. Eur J Pharmacol 906:174200. https://doi.org/10.1016/j.ejphar.2021.174200
13. Yao J, Li J, Gao L, He Y, Xie J, Zhu P, Zhang Y, Zhang X, Duan L, Yang S, Song C, Shu X (2022) Epidemiological investigation and genetic analysis of pseudorabies virus in Yunnan Province of China from 2017 to 2021. Viruses 14:895. https://doi.org/10.3390/v14050895
14. Shu X, Zhang Y, Zhang X, Zhang Y, Shu Y, Wang Y, Zhang Z, Song C (2024) Therapeutic and immune-regulation effects of *Scutellaria baicalensis* Georgi polysaccharide on pseudorabies in piglets. Front Vet Sci 11:1356819. https://doi.org/10.3389/fvets.2024.1356819
15. Li Y, Chopp M, Chen J, Wang L, Gautam SC, Xu YX, Zhang Z (2000) Intrastriatal transplantation of bone marrow nonhematopoietic cells improves functional recovery after stroke in adult mice. J Cereb Blood Flow Metab 20:1311–1319. https://doi.org/10.1097/00004647-200009000-00006
16. Zhang L, Wang Y, Xiayu X, Shi C, Chen W, Song N, Fu X, Zhou R, Xu YF, Huang L, Zhu H, Han Y, Qin C (2017) Altered gut microbiota in a mouse model of Alzheimer's disease. J Alzheimers Dis 60:1241–1257. https://doi.org/10.3233/JAD-170020
17. Radu M, Chernoff J (2013) An in vivo assay to test blood vessel permeability. J Vis Exp 73:e50062. https://doi.org/10.3791/50062
18. Verma S, Lo Y, Chapagain M, Lum S, Kumar M, Gurjav U, Luo H, Nakatsuka A, Nerurkar VR (2009) West Nile virus infection modulates human brain microvascular endothelial cells tight junction proteins and cell adhesion molecules: transmigration across the in vitro blood-brain barrier. Virology 385:425–433. https://doi.org/10.1016/j.virol.2008.11.047
19. Zhou Y, Zhou B, Pache L, Chang M, Khodabakhshi AH, Tanaseichuk O, Benner C, Chanda SK (2019) Metascape provides a biologist-oriented resource for the analysis of systems-level datasets. Nat Commun 10:1523. https://doi.org/10.1038/s41467-019-09234-6
20. Yao L, Xue X, Yu P, Ni Y, Chen F (2018) Evans blue dye: a revisit of its applications in biomedicine. Contrast Media Mol Imaging 2018:7628037. https://doi.org/10.1155/2018/7628037
21. Li JS, Liu JX, Yu HB, Wang D (2006) Establishment and evaluation of reproduction of middle cerebral artery occlusion to produce cerebral ischemia with autologous blood clot and nylon thread in rat. Zhongguo Wei Zhong Bing Ji Jiu Yi Xue 18:272–274 (in Chinese)
22. Cathcart J, Pulkoski-Gross A, Cao J (2015) Targeting matrix metalloproteinases in cancer: bringing new life to old ideas. Genes Dis 2:26–34. https://doi.org/10.1016/j.gendis.2014.12.002
23. Ralay RH, Hodge JN, Choi N, Wainwright MS (2012) Albumin induces upregulation of matrix metalloproteinase-9 in astrocytes via MAPK and reactive oxygen species-dependent pathways. J Neuroinflammation 9:68. https://doi.org/10.1186/1742-2094-9-68
24. Feng D, Zhou J, Liu H, Wu X, Li F, Zhao J, Zhang Y, Wang L, Chao M, Wang Q, Qin H, Ge S, Liu Q, Zhang J, Qu Y (2022) Astrocytic NDRG2-PPM1A interaction exacerbates blood-brain barrier disruption after subarachnoid hemorrhage. Sci Adv 8:q2423. https://doi.org/10.1126/sciadv.abq2423
25. Dean HJ, Miller JM, Ackermann MR, Gao XY, Anderson LL, Jacobson CD, Cheung AK (1996) Replication and pathogenicity after intranasal and intracranial inoculation of swine with a recombinant pseudorabies virus containing a deletion at the UL/IR junction. Virology 223:19–28. https://doi.org/10.1006/viro.1996.0451
26. Zhai X, Zhao W, Li K, Zhang C, Wang C, Su S, Zhou J, Lei J, Xing G, Sun H, Shi Z, Gu J (2019) Genome characteristics and evolution of pseudorabies virus strains in Eastern China from 2017 to 2019. Virol Sin 34:601–609. https://doi.org/10.1007/s12250-019-00140-1

27. Yang QY, Sun Z, Tan FF, Guo LH, Wang YZ, Wang J, Wang ZY, Wang LL, Li XD, Xiao Y, Tian KG (2016) Pathogenicity of a currently circulating Chinese variant pseudorabies virus in pigs. World J Virol 5:23–30. https://doi.org/10.5501/wjv.v5.i1.23
28. van Oirschot JT, Gielkens AL (1984) Some characteristics of four attenuated vaccine virus strains and a virulent strain of Aujeszky's disease virus. Vet Q 6:225–229. https://doi.org/10.1080/01652176.1984.9693940
29. Takahashi H, Yoshikawa Y, Kai C, Yamanouchi K (1993) Mechanism of pruritus and peracute death in mice induced by pseudorabies virus (PRV) infection. J Vet Med Sci 55:913–920. https://doi.org/10.1292/jvms.55.913
30. Klopfleisch R, Klupp BG, Fuchs W, Kopp M, Teifke JP, Mettenleiter TC (2006) Influence of pseudorabies virus proteins on neuroinvasion and neurovirulence in mice. J Virol 80:5571–5576. https://doi.org/10.1128/JVI.02589-05
31. Babic N, Klupp B, Brack A, Mettenleiter TC, Ugolini G, Flamand A (1996) Deletion of glycoprotein gE reduces the propagation of pseudorabies virus in the nervous system of mice after intranasal inoculation. Virology 219:279–284. https://doi.org/10.1006/viro.1996.0247
32. Wu H, Qi H, Wang B, Li M, Qu L, Li S, Luo Y, Li LF, Zheng GL, Qiu HJ, Sun Y (2023) The mutations on the envelope glycoprotein D contribute to the enhanced neurotropism of the pseudorabies virus variant. J Biol Chem 299:105347. https://doi.org/10.1016/j.jbc.2023.105347
33. Damann N, Klopfleisch R, Rothermel M, Doerner JF, Mettenleiter TC, Hatt H, Wetzel CH (2006) Neuronal pathways of viral invasion in mice after intranasal inoculation of pseudorabies virus PrV-9112C2 expressing bovine herpesvirus 1 glycoprotein B. J Neurovirol 12:60–64. https://doi.org/10.1080/13550280500516450
34. Song C, Ye H, Zhang X, Zhang Y, Li Y, Yao J, Gao L, Wang S, Yu Y, Shu X (2024) Isolation and characterization of yunnan variants of the pseudorabies virus and their pathogenicity in rats. Viruses 16:233. https://doi.org/10.3390/v16020233
35. Tan L, Yao J, Yang Y, Luo W, Yuan X, Yang L, Wang A (2021) Current status and challenge of pseudorabies virus infection in China. Virol Sin 36:588–607. https://doi.org/10.1007/s12250-020-00340-0
36. Profaci CP, Munji RN, Pulido RS, Daneman R (2020) The blood-brain barrier in health and disease: Important unanswered questions. J Exp Med 217:e20190062. https://doi.org/10.1084/jem.20190062
37. Liebner S, Dijkhuizen RM, Reiss Y, Plate KH, Agalliu D, Constantin G (2018) Functional morphology of the blood-brain barrier in health and disease. Acta Neuropathol 135:311–336. https://doi.org/10.1007/s00401-018-1815-1
38. Knowland D, Arac A, Sekiguchi KJ, Hsu M, Lutz SE, Perrino J, Steinberg GK, Barres BA, Nimmerjahn A, Agalliu D (2014) Stepwise recruitment of transcellular and paracellular pathways underlies blood-brain barrier breakdown in stroke. Neuron 82:603–617. https://doi.org/10.1016/j.neuron.2014.03.003
39. Feige L, Zaeck LM, Sehl-Ewert J, Finke S, Bourhy H (2021) Innate immune signaling and role of glial cells in herpes simplex virus- and rabies virus-induced encephalitis. Viruses 13:2364. https://doi.org/10.3390/v13122364
40. Erickson MA, Banks WA (2022) Transcellular routes of blood-brain barrier disruption. Exp Biol Med 247:788–796. https://doi.org/10.1177/15353702221080745
41. Zhang L, Zhou L, Bao L, Liu J, Zhu H, Lv Q, Liu R, Chen W, Tong W, Wei Q, Xu Y, Deng W, Gao H, Xue J, Song Z, Yu P, Han Y, Zhang Y, Sun X, Yu X, Qin C (2021) SARS-CoV-2 crosses the blood-brain barrier accompanied with basement membrane disruption without tight junctions alteration. Signal Transduct Target Ther 6:337. https://doi.org/10.1038/s41392-021-00719-9
42. Zou SS, Zou QC, Xiong WJ, Cui NY, Wang K, Liu HX, Lou WJ, Higazy D, Zhang YG, Cui M (2021) Brain microvascular endothelial cell-derived HMGB1 facilitates monocyte adhesion and transmigration to promote JEV neuroinvasion. Front Cell Infect Microbiol 11:701820. https://doi.org/10.3389/fcimb.2021.701820
43. Liu M, Li H, Zhang L, Xu Z, Song Y, Wang X, Chu R, Xiao Y, Sun M, Ma Y, Mi W (2021) Cottonseed oil alleviates ischemic stroke-induced oxidative stress injury via activating the Nrf2 signaling pathway. Mol Neurobiol 58:2494–2507. https://doi.org/10.1007/s12035-020-02256-y
44. Guttenplan KA, Weigel MK, Prakash P, Wijewardhane PR, Hasel P, Rufen-Blanchette U, Münch AE, Blum JA, Fine J, Neal MC, Bruce KD, Gitler AD, Chopra G, Liddelow SA, Barres BA (2021) Neurotoxic reactive astrocytes induce cell death via saturated lipids. Nature 599:102–107. https://doi.org/10.1038/s41586-021-03960-y
45. Boghdadi AG, Teo L, Bourne JA (2020) The neuroprotective role of reactive astrocytes after central nervous system injury. J Neurotrauma 37:681–691. https://doi.org/10.1089/neu.2019.6938
46. Villarino AV, Kanno Y, O'Shea JJ (2017) Mechanisms and consequences of Jak-STAT signaling in the immune system. Nat Immunol 18:374–384. https://doi.org/10.1038/ni.3691
47. Sarmiento SM, Larkin JR, Martin C, Khrapitchev AA, Maczka M, Economopoulos V, Scott H, Escartin C, Bonvento G, Serres S, Sibson NR (2020) STAT3-mediated astrocyte reactivity associated with brain metastasis contributes to neurovascular dysfunction. Cancer Res 80:5642–5655. https://doi.org/10.1158/0008-5472.CAN-20-2251
48. Hu Q, Bian Q, Rong D, Wang L, Song J, Huang HS, Zeng J, Mei J, Wang PY (2023) JAK/STAT pathway: Extracellular signals, diseases, immunity, and therapeutic regimens. Front Bioeng Biotechnol 11:1110765. https://doi.org/10.3389/fbioe.2023.1110765
49. Kaur G, Lungarella G, Rahman I (2020) SARS-CoV-2 COVID-19 susceptibility and lung inflammatory storm by smoking and vaping. J Inflamm 17:21. https://doi.org/10.1186/s12950-020-00250-8
50. Lin Y, Liu S, Sun Y, Chen C, Yang S, Pei G, Lin M, Yu J, Liu X, Wang H, Long J, Yan Q, Liang J, Yao J, Yi F, Meng L, Tan Y, Chen N, Yang Y, Ai Q (2024) CCR5 and inflammatory storm. Ageing Res Rev 96:102286. https://doi.org/10.1016/j.arr.2024.102286
51. Ozgurbuz U, Kabadayi EH, Akogullari CD, Vatansever HS (2023) Favipiravir protects enterocytes from cell death after inflammatory storm. Cureus 15:e47417. https://doi.org/10.7759/cureus.47417
52. Li F, Wang Y, Yu L, Cao S, Wang K, Yuan J, Wang C, Wang K, Cui M, Fu ZF (2015) Viral infection of the central nervous system and neuroinflammation precede blood-brain barrier disruption during Japanese encephalitis virus infection. J Virol 89:5602–5614. https://doi.org/10.1128/JVI.00143-15
53. Krasemann S, Haferkamp U, Pfefferle S, Woo MS, Heinrich F, Schweizer M, Appelt-Menzel A, Cubukova A, Barenberg J, Leu J, Hartmann K, Thies E, Littau JL, Sepulveda-Falla D, Zhang L, Ton K, Liang Y, Matschke J, Ricklefs F, Sauvigny T, Sperhake J, Fitzek A, Gerhartl A, Brachner A, Geiger N, König EM, Bodem J, Franzenburg S, Franke A, Moese S, et al. (2022) The blood-brain barrier is dysregulated in COVID-19 and serves as a CNS entry route for SARS-CoV-2. Stem Cell Rep 17:307–320. https://doi.org/10.1016/j.stemcr.2021.12.011

Publisher's Note